The Astrophysical Journal, 833:226 (16pp), 2016 December 20 doi:10.3847/1538-4357/833/2/226

THE *GALEX* TIME DOMAIN SURVEY. II. WAVELENGTH-DEPENDENT VARIABILITY OF ACTIVE GALACTIC NUCLEI IN THE PAN-STARRS1 MEDIUM DEEP SURVEY

T. Hung[1], S. Gezari[1], D. O. Jones[2], R. P. Kirshner[3], R. Chornock[4], E. Berger[3], A. Rest[5], M. Huber[6], G. Narayan[7], D. Scolnic[8], C. Waters[6], R. Wainscoat[6], D. C. Martin[9], K. Forster[9], and J. D. Neill[9]
[1] Department of Astronomy, University of Maryland, College Park, MD 20742, USA
[2] Department of Physics and Astronomy, Johns Hopkins University, Baltimore, MD 21218, USA
[3] Harvard-Smithsonian Center for Astrophysics, 60 Garden Street, Cambridge, MA 02138, USA
[4] Astrophysical Institute, Department of Physics and Astronomy, 251B Clippinger Lab, Ohio University Athens, OH 45701, USA
[5] Space Telescope Science Institute, 3700 San Martin Drive, Baltimore, MD 21218, USA
[6] Institute for Astronomy, University of Hawaii, 2680 Woodlawn Drive, Honolulu, HI 96822, USA
[7] National Optical Astronomy Observatory, 950 North Cherry Avenue, Tucson, AZ 85719, USA
[8] Kavli Institute for Cosmological Physics, University of Chicago, Chicago, IL 60637, USA
[9] Cahill Center for Astrophysics, California Institute of Technology, 1216 East California Boulevard, Mail Code 278-17, Pasadena, California 91125, USA
Received 2016 June 27; revised 2016 August 22; accepted 2016 September 20; published 2016 December 19

ABSTRACT

We analyze the wavelength-dependent variability of a sample of spectroscopically confirmed active galactic nuclei selected from near-UV (NUV) variable sources in the *GALEX* Time Domain Survey that have a large amplitude of optical variability (difference-flux S/N $>$ 3) in the Pan-STARRS1 Medium Deep Survey (PS1 MDS). By matching *GALEX* and PS1 epochs in five bands (NUV, g_{P1}, r_{P1}, i_{P1}, z_{P1}) in time, and taking their flux difference, we create co-temporal difference-flux spectral energy distributions (ΔfSEDs) using two chosen epochs for each of the 23 objects in our sample, on timescales of about a year. We confirm the "bluer-when-brighter" trend reported in previous studies, and measure a median spectral index of the ΔfSEDs of $\alpha_\lambda = 2.1$ that is consistent with an accretion disk spectrum. We further fit the ΔfSEDs of each source with a standard accretion disk model in which the accretion rate changes from one epoch to the other. In our sample, 17 out of 23 ($\sim$74%) sources are described well by this variable accretion-rate disk model, with a median average characteristic disk temperature $\bar{T}^*$ of 1.2×10^5 K that is consistent with the temperatures expected, given the distribution of accretion rates and black hole masses inferred for the sample. Our analysis also shows that the variable accretion rate model is a better fit to the ΔfSEDs than a simple power law.

Key words: accretion, accretion disks – black hole physics – galaxies: nuclei – surveys – ultraviolet: general

1. INTRODUCTION

Active galactic nuclei (AGNs) are known to vary across the observable electromagnetic spectrum on timescales ranging from seconds to years. Large time-domain surveys (TDSs) have confirmed variability as a ubiquitous characteristic of AGN (e.g., Vanden Berk et al. 2004; Wilhite et al. 2005), ruling out models involving extrinsic factors such as gravitational microlensing, star collisions, or multiple supernovae or starbursts near the nucleus (Kokubo 2015 and references therein). In particular, the origin of UV/optical variability is of great interest for its connection to the AGN central engine, because the UV/optical continuum is thought to arise directly from the accretion disk around a supermassive black hole.

A well-established characteristic of AGN UV/optical variability is the "bluer-when-brighter" trend, in which the source is bluer in the bright state than in the faint state (Vanden Berk et al. 2004; Wilhite et al. 2005; Schmidt et al. 2012). (Albeit, a reverse trend was observed for low-luminosity AGN in Heinis et al. 2016). However, the interpretation of the "bluer-when-brighter" trend is still under debate. Whether or not the intrinsic AGN color becomes bluer when it brightens, or if the red color in a low state is caused by contamination from a non-variable component (e.g., host galaxy flux) (Winkler et al. 1992), cannot be distinguished due to the difficulties of separating host galaxy light from the AGN.

Kelly et al. (2009) found that the optical variability of an AGN is well-described by a damped random walk (DRW) process, with model-fit timescales that are consistent with the thermal timescale of an accretion disk. A similar conclusion was reached by MacLeod et al. (2010), with a sample of $\sim$9000 spectroscopically confirmed quasars in SDSS Stripe 82. Furthermore, MacLeod et al. (2010) found that the variability amplitude was anti-correlated with Eddington ratio, implying that the mechanism driving the optical variability was related to the accretion disk.

Several prevailing models for the origin of UV/optical variability in the AGN accretion disk include thermal reprocessing of X-ray emission (Krolik et al. 1991), changes in the mass accretion rate (e.g., Pereyra et al. 2006; Li & Cao 2008), and an extremely inhomogeneous accretion disk (Dexter & Agol 2011; Ruan et al. 2014). In an effort to examine these models, several studies have been carried out. For example, Ruan et al. (2014) found that a relative spectral variability composite spectrum constructed from SDSS quasars is better fit with an inhomogeneous disk model consisting of multiple zones undergoing independent temperature fluctuations, rather than simply changes in a steady-state mass accretion rate. Although the localized temperature fluctuations may arise from magnetorotational instabilities in an accretion flow (see discussions in Hirose et al. 2009; Janiuk & Misra 2012; Jiang et al. 2013), it has also been pointed out by Kokubo (2015) that the inhomogeneous disk model predicts a weak inter-band correlation, which is contradictory to what is often observed in the SDSS quasar light curves. Kokubo (2015) attributed the successful fitting result in Ruan et al. (2014) to the use of a composite difference spectrum, in which the

superposition of localized flares at different radii smears out the inter-band flux-flux correlation in individual quasars.

On the other hand, Pereyra et al. (2006, hereafter P06) presented the first successful result of fitting a composite difference spectrum of SDSS quasars to a standard thin disk model (Shakura & Sunyaev 1973) with changes in accretion rate from one epoch to the next. Recently, many works that try to explain AGN variability have also reached conclusions that are supportive of this variable accretion rate model (Li & Cao 2008; Sakata et al. 2011). The model suggests that the "bluer when brighter" trend is caused by intrinsic AGN spectral hardening. The same conclusion was reached in Wilhite et al. (2005), where they found steeper spectral index in the composite flux difference spectrum than that in the composite spectrum. Despite the elegance of this model, there is a discrepancy between the AGN UV-optical variability timescale and the sound crossing and viscous timescales (by a factor of 10^3, see discussion in Section 6.3) of the accretion disk. Furthermore, Schmidt et al. (2012), Kokubo et al. (2014) reported that on the timescales of years, characteristic optical color variability in individual SDSS stripe 82 quasars is larger than the color variability predicted by a steady-state accretion disk with a varying accretion rate.

In this paper, we continue the investigation of the origin of UV/optical variability in quasars, with several improvements. We apply the variable accretion rate model (P06) to the difference-flux spectral energy distributions (SEDs) of individual quasars instead of using a composite quasar difference spectrum, and over a wavelength range broader than previous optical studies (≈1700–9000 Å in observer's frame), thanks to the nearly simultaneous near-UV (NUV) observations from *GALEX*. The sample of AGNs and quasars investigated in this paper is selected from NUV-variability from the *GALEX* TDS and is analyzed using broad-band *GALEX* NUV and Pan-STARRS1 Medium Deep Survey (PS1 MDS) optical *griz* photometric data. In Section 2, we describe the sample selection and the spectroscopic data used in this paper. We describe details of the P06 model in Section 3. The creation of Δf SEDs, the spectral fitting procedures, and the derivation of fundamental AGN parameters are detailed in Figure 4.1. We present our result in Section 5. The implications of the results are discussed in Section 6.

2. SAMPLE SELECTION AND DATA REDUCTION

Throughout the analysis in this paper, we define an AGN as an optical stochastic variable source with extended host morphology, whereas quasars are defined as optical point sources with the following colors (Gezari et al. 2013).

$$\begin{aligned} u - g &< 0.7 \\ -0.1 < g - r &< 1.0. \end{aligned} \quad (1)$$

The optical morphology classification and colors are obtained from CFHT u band and the PS1 deep stack catalog (*griz*) in Heinis et al. (2016). The classification of stochastic variablility was carried out in Kumar et al. (2015) by comparing the goodness of fit of the light curves to the Ornstein-Uhlenbeck process, a general version of the DRW, and the light curve shapes characteristic of supernovae.

We cross-match the *GALEX* TDS UV-variable source catalog with the PS1 transient alert database, using a search radius of 2″, to obtain a sample of 335 UV and optical variable sources. For the analysis, we select a subsample of 24 large-amplitude optically variable sources with a difference-flux signal-to-noise (S/N) > 3 in the g band, all of which we have spectra for. All but one source in this subsample are spectroscopically classified as active galaxies, with 11 classified as AGN and 12 classified as quasars using our definitions described above. Spectroscopy shows that the exception is a normal galaxy with unusual UV variability (see Section 6.2 for discussion).

2.1. GALEX TDS

GALEX TDS (Gezari et al. 2013) covered ∼40 deg^2 of the sky and detected over 1000 UV variable sources with observations that span a three-year baseline, with a cadence of two days. *GALEX* TDS fields were designed to monitor 6 out of 10 PS1 MDS fields, with 7 *GALEX* TDS pointings at a time to cover the 8 deg^2 field of view of PS1. The typical exposure time per epoch is 1.5 ks (or a 5σ point-source limit of $m_{AB} \sim$ 23.3 mag). The *GALEX* far-UV (FUV) detector became non-operational during the time of the full survey, and so only near-UV (NUV) data is available for analysis.

Sources were classified as NUV variable in the *GALEX* TDS catalog if they have at least one epoch in which $|m_k - \bar{m}| > 5\sigma(\bar{m}, k)$ (Gezari et al. 2013), where m_k is the magnitude of epoch k and $\bar{m}$ is calculated only from epochs that have a magnitude above the detection limit of that epoch. The variable sources were then classified using a combination of optical host colors and morphology, UV light curves, and matches to archival X-ray and spectroscopy catalogs. The final sample of 1078 NUV variable sources consists of 62% active galaxies (AGN and quasars), 10% variable stars (RR Lyrae, M dwarfs, and cataclysmic variables), and the rest are sources without classification (generally without spectra).

2.2. PS1 MDS

The Pan-STARRS1 Medium Deep Survey (PS1 MDS) surveyed 10 spatially separated fields, each with a 8 deg^2 field of view, with a set of five broadband filters: g_{P1}, r_{P1}, i_{P1}, z_{P1}, y_{P1} (Kaiser et al. 2010). The average cadence was six epochs in 10 days, with a 5σ depth of $m_{AB} \sim$ 23.1 mag, 23.3 mag, 23.2 mag, 22.8 mag in g_{P1}, r_{P1}, i_{P1}, and z_{P1}, respectively (Rest et al. 2014). Each night, five MD fields were observed with a three-day staggered cadence in each filter with the following pattern: g_{P1} and r_{P1} in the same night (dark time), followed by i_{P1} and z_{P1} on the subsequent second and third night, respectively. During the week of the full moon, the y_{P1} band was observed exclusively. We do not use the y_{P1} band in our analysis, due to the large time interval between y_{P1} and the other bands.

We use data from the transient alert system of PS1 MDS that is designed to detect transient events. The images taken in PS1 MDS are detrended by the Image Processing Pipeline (IPP) (Magnier 2006). Typically, eight dithered images are taken per filter and stacked in a given night. Image subtraction of a template created from observations of two earlier epochs from the nightly stacked image is performed with the `photpipe` pipeline (Rest et al. 2005). The system determines the spatially varying convolution kernel in a robust way before performing a subtraction of the two images. A transient detection is flagged if it shows positive detections with a signal-to-noise ratio (S/N) ⩾ 4 in at least three $griz_{P1}$ images within a time window of 10 days. Note that most previous studies of AGN variability have used samples of point-like quasars, but avoided AGN

with resolved galaxy hosts because the host galaxy light is hard to separate from the AGN light. With difference imaging, the non-variable component can be removed effectively, leaving only the variable component of the AGN.

2.3. Optical Spectra

We gather spectra for all the objects in our sample, including five from the first data release of the Sloan Digital Sky Survey (Abazajian et al. 2003 SDSS DR1;), eight from the archival Baryon Oscillation Spectroscopic Survey (BOSS; Dawson et al. 2013), one from the archival 2dF Galaxy Redshift Survey (2dFGRS) (2dFGRS; Colless et al. 2003), and the remaining ten from the PS1 transients follow-up programs (PI Kirshner and PI Berger) using MMT Hectospec.

The SDSS spectra were observed with a 2.5 m telescope and a pair of fiber-fed double spectrographs at the Apache Point Observatory. Each SDSS spectrum is measured from 3800 Å to 9200 Å on 2048 × 2048 CCDs with a resolving power ($\lambda/\Delta\lambda$) of ∼2000.

Hectospec is a multi-fiber spectrograph mounted on MMT that is capable of observing 300 objects simultaneously (Fabricant et al. 2005). During the observation, a 270 (lpmm) grating was used, which corresponds to a dispersion of 1.21 Å/pix near 5000 Å. The spectral coverage is from 3650 to 9200 Å.

The spectra of SDSS were extracted and calibrated with its own `spectro2d` pipeline, whereas the MMT spectra were reduced with the automated `HSRED` pipeline, which is an `IDL` package based on the reduction routines of SDSS spectroscopic data. The optical spectra were reduced following a conventional reduction protocal that includes bias removal, flat fielding, cosmic ray removal, sky subtraction, 1-d spectrum extraction, and wavelength and flux calibration.

The 2dFGRS is a large spectroscopic survey conducted using the Two-Degree Field (2dF) multi-fiber spectrograph at the Anglo-Australian telescope. The survey spectra cover the wavelength range of 3600–8000 Å with a resolution of 9 Å. Due to the lack of flux calibration files for the 2dFGRS spectra, we can only approximate the relative flux by dividing the 2dFGRS spectra by a response curve created from observing a set of stars with SDSS *ugriz* photometry (Baldry et al. 2002).

3. ACCRETION DISK MODEL

Pereyra et al. (2006) successfully modeled a composite residual spectrum of over 300 SDSS quasars with a standard disk model in which the mass accretion rate changes from one epoch to another. In this paper, we attempt to take this further by fitting ΔfSEDs with the P06 model on an object per object basis.

In the standard geometrically thin and optically thick accretion disk model (Shakura & Sunyaev 1973), the potential energy released as the mass accretes onto a black hole is emitted locally. Considering the interplay between mass moving inward and shear stresses transporting angular momentum outward, the disk temperature profile can be described by

$$T(r) = T^* \left(\left(\frac{r_i}{r} \right)^3 \left[1 - \left(\frac{r_i}{r} \right)^{1/2} \right] \right)^{1/4}, \quad (2)$$

where r_i is the inner disk radius and T^* is the characteristic temperature defined by

$$T^* = \left(\frac{3GM_{\rm bh}\dot{M}_{\rm accr}}{8\pi r_i^3 \sigma} \right)^{1/4}, \quad (3)$$

where G is the gravitational constant, $M_{\rm bh}$ is the black hole mass, and $\dot{M}_{\rm accr}$ is the mass accretion rate.

If we assume the inner disk radius r_i to be the radius of the innermost stable circular orbit ($R_{\rm ISCO} = 6GM_{\rm bh}/c^2$) around a Schwarzschild black hole, the characteristic temperature T^* becomes

$$T^* = \left(\frac{\dot{M}_{\rm accr} c^6}{576\pi G^2 M_{\rm bh}^2 \sigma_s} \right)^{1/4}. \quad (4)$$

Because $M_{\rm bh}$ should not change significantly on a timescale of years, changes in T^* trace changes in accretion rate.

For a given temperature profile, flux from the disk is given by the sum over blackbody spectra of annuli. The total flux from both sides of the disk is given by

$$f_\lambda(T^*) = \int_{r_i}^{\infty} \pi \frac{\frac{2hc^2}{\lambda^5}}{\exp\left(\frac{hc}{\lambda kT^* t(r/r_i)}\right) - 1} 4\pi r \, dr, \quad (5)$$

where c is the speed of light, h is Planck's constant, k is Boltzmann's constant, and the function $t(x) = x^{-3}(1 - x^{-1/2})^{1/4}$ defines

$$s \equiv \frac{r}{r_i}. \quad (6)$$

We can rewrite the expression for flux by normalizing the disk radius to the inner disk radius to:

$$f_\lambda(T^*) = r_i^2 \int_1^{\infty} \pi \frac{\frac{2hc^2}{\lambda^5}}{\exp\left(\frac{hc}{\lambda kT^* t(s)}\right) - 1} 4\pi s \, ds. \quad (7)$$

The observed disk flux can be expressed as

$$f_{o\lambda} = c_o \, g_\lambda(T^*), \quad (8)$$

where c_o is a constant that depends on the black hole mass (see definition of $R_{\rm ISCO}$), the object's cosmological distance, and the disk viewing angle and $g_\lambda(T^*)$ is defined as the integral in Equation (7).

$$g_\lambda(T^*) \equiv \int_1^{\infty} \pi \frac{\frac{2hc^2}{\lambda^5}}{\exp\left(\frac{hc}{\lambda kT^* t(s)}\right) - 1} 4\pi s \, ds. \quad (9)$$

l

The P06 model assumes the disk evolved from one steady state to the other, between two arbitrary epochs, with a change in mass accretion rate $\Delta\dot{M}_{\rm accr}$. The observed flux difference is then

$$\Delta f_{o\lambda} = c_o(g_\lambda(T_2^*) - g_\lambda(T_1^*)), \quad (10)$$

with a mean characteristic temperature that is defined as

$$\bar{T}^* = \frac{1}{2}(T_2^* + T_1^*), \quad (11)$$

and

$$\Delta T^* = T_2^* - T_1^*. \quad (12)$$

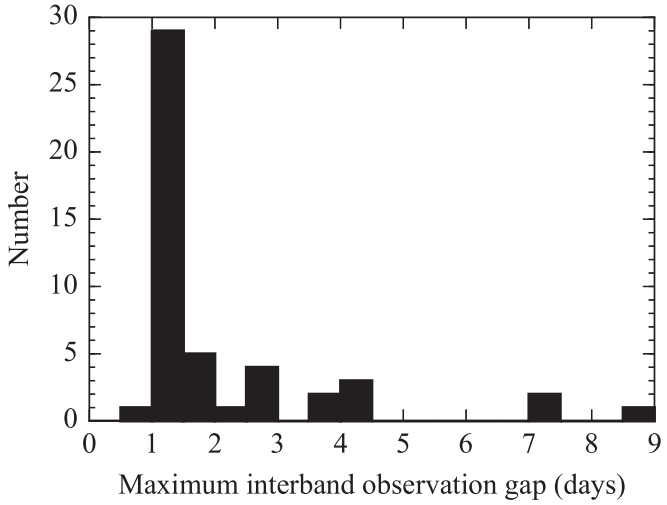

Figure 1. Distribution of the maximum obervation gap between NUV and the optical bands of the two epochs used to construct Δf SEDs in our sample.

P06 performed Taylor expansion about $\bar{T}^*$ for $g_\lambda(T_1^*)$ and $g_\lambda(T_2^*)$ and reduced Equation (10) to its primary term

$$\Delta f_{o\lambda} \approx c_o \, \Delta T^* \frac{\partial g_\lambda}{\partial T^*}\bigg|_{\bar{T}*} . \quad (13)$$

One thing to note here is that T_1^* and T_2^* cannot be determined individually. Because the partial derivative term here is a function of $\bar{T}^*$, one would expect to find pairs of T_1^* and T_2^* that have the same $\bar{T}^*$ corresponding to several local minima in χ^2 space. To avoid problems caused by this degeneracy, we only fit the mean characteristic temperature $\bar{T}^*$ in this work.

4. ANALYSIS

Our analysis consists of three steps: (1) selecting a sample of objects with a bright and a faint phase that have synchronous interband observations for each object, (2) constructing the difference-flux SED using the two chosen epochs, and (3) fitting the Δf SEDs with the P06 model (Equation (13)). The free parameters in the P06 model are $\bar{T}^*$ and an arbitrary normalization constant.

4.1. Bright and Faint Phase

Cross-matching *GALEX* NUV and PS1 *griz* data for studying time variable phenomena can be tricky because the observations were not made at the same time for different telescopes and filters. To preserve the simultaneity of the data, we first group each *GALEX* epoch with PS1 by minimizing the interband observation gap with respect to *GALEX* NUV. For each object, the two best-aligned *GALEX* epochs with *griz* observations within nine days of the NUV observation are chosen as their bright and faint epochs, where bright and faint are decided by the NUV magnitude.

Next, we take the flux difference between the bright and the faint epochs for each object and propagate the uncertainties to calculate the S/N for the difference-flux (Δf). We exclude the small optical variability epochs with a Δf S/N lower than 3 in the g band. Among the 335 objects that have overlapped in both *GALEX* and PS1 surveys, we found a sample of 24 objects that have more than one co-temporaneous observations between all five bands and have large amplitude of variability (S/N(Δf_g) > 3) between these two chosen epochs. Figure 1 shows the distribution of the largest observation gaps in each faint and bright epoch for all 24 objects. Most of the epochs used for our analyses have nearly simultaneous observations across NUV and optical bands.

4.2. Construction of the Difference-flux SEDs

Once the bright and faint epochs are determined, we reprocess the image subtraction to obtain more accurate flux measurements at the two chosen epochs using a customized pipeline developed by D. O. Jones et al. (2016, in preparation). Unlike the templates used in `photpipe`, which are created from stacking observations of two earlier epochs resulting in double the typical exposure time of the science epoch, the templates in D. O. Jones et al. (2016, in preparation) stack images from every season except the season the event was discovered in (~70 images). This pipeline then performs forced photometry on stars in each field to determine the zeropoints of each image after determining accurate stellar centroids using average positions from over 300 individual images. The new pipeline also increased the number of stars used to build the point-spread function (PSF) model to improve the fit and reduce the photometric noise.

It is worth noting that the *GALEX* NUV magnitudes are aperture magnitudes extracted using a 6″ radius aperture that include the host flux, whereas the PS1 $g_{\rm P1}r_{\rm P1}i_{\rm P1}z_{\rm P1}$ magnitudes are measured after difference imaging, where flux from an earlier template has been subtracted off. We did not perform image differencing on *GALEX* images because most galaxies are unresolved by the *GALEX* NUV 5.″3 FWHM PSF. When we construct a Δf SED, we subtract the flux in each band in the faint epoch from the bright epoch in flux space, so that we are only sensitive to the SED of the change in flux (Δf) between the two epochs, and we are insensitive to which template was used to construct the PS1 difference magnitude.

The flux subtraction is performed in flux density units (erg s^{-1} cm^{-2} $Å^{-1}$) to match the model prediction in $f_\lambda - \lambda$ space. We demonstrate the construction of Δf SEDs in Figure 3, which shows the light curve of COSMOS_MOS23-10, with vertical dashed lines marking the two *GALEX* epochs that correspond to the faint and bright phase. The horizontal lines denote the reference magnitude of each filter at the faint epoch.

In Figure 2, we show in each PS1 *griz* band the distribution of flux change of any pair of observations with time intervals of 3 ± 0.5 days, 9 ± 0.5 days, 30 ± 0.5 days, and 365 ± 0.5 days. The standard deviation of the distribution for each time interval, which measures the amplitude of variability for the given timescale, is indicated by σ_3, σ_9, σ_{30}, and σ_{365} in Figure 2. From the distribution, we find the variability in g band being more sensitive to timescale than the other three filters.

The measurement uncertainty given by our pipeline is comparable to σ_3 in each PS1 band. Although three objects in our sample have interband observation gap as large as 7–9 days, we see in Figure 2 that σ_9 is only ~36% greater than σ_3. We find the difference insignificant compared to the uncertainties introduced by subtracting against a bright host galaxy, which can increase the measurement error by a factor of 2.

4.3. Galactic Extinction Correction

We correct for Galactic extinction before performing model fitting to our difference spectra. For *GALEX* NUV data, we use

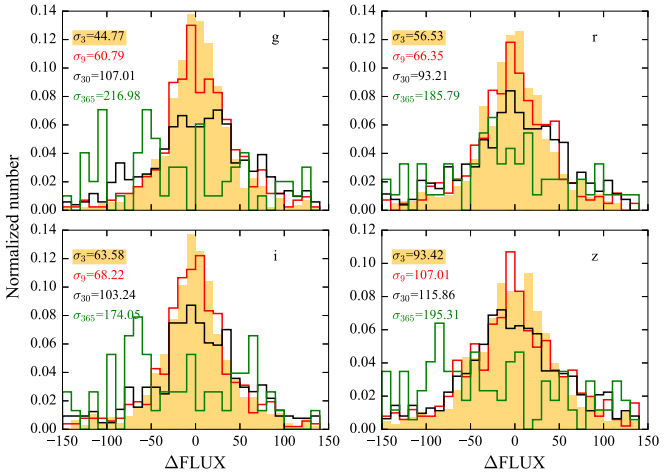

Figure 2. Distribution of flux difference in four different Δt bins: 3 ± 0.5 days (orange filled), 9 ± 0.5 days (red), 30 ± 0.5 days (black), 365 ± 0.5 days (green) in PS1 *griz* bands. The flux used here corresponds to a zeropoint of 27.5. The histograms are normalized by the total number of pairs in each Δt bin.

the band extinction given in Wyder et al. (2007) that is computed by assuming the Cardelli et al. (1989) extinction law and $R_V = 3.1$.

$$A(NUV)/E(B-V) = 8.2 \tag{14}$$

On the other hand, the Galactic extinction of each PS1 band is computed as a function of PS1 stellar color with Fitzpatrick (1999) extinction law using $R_V = 3.1$ by Tonry et al. (2012). The Galactic extinctions of PS1 bands are given as follows:

$$\begin{aligned} A(g_{\rm P1})/E(B-V) &= 3.613 - 0.0972(g_{\rm P1} - i_{\rm P1}) \\ &\quad + 0.0100(g_{\rm P1} - i_{\rm P1})^2 \\ A(r_{\rm P1})/E(B-V) &= 2.585 - 0.0315(g_{\rm P1} - i_{\rm P1}) \\ A(i_{\rm P1})/E(B-V) &= 1.908 - 0.0152(g_{\rm P1} - i_{\rm P1}) \\ A(z_{\rm P1})/E(B-V) &= 1.499 - 0.0023(g_{\rm P1} - i_{\rm P1}) \end{aligned} \tag{15}$$

We use the $E(B-V)$ value from Schlegel et al. (1998) dust map together with Equations (14) and (15) to correct for the Galactic extinction in our difference spectra.

4.4. Fitting the Difference-flux SEDs

We use Equation (13) to fit the observed Δf SEDs in the rest frame. The partial derivative may be further simplified to

$$\left.\frac{\partial g_\lambda}{\partial T^*}\right|_{\bar{T}*} = \frac{\pi\, 2h^2c^3}{\lambda^6 k \bar{T}^{*2}} \int_1^\infty \frac{t(s)}{\left(\exp\left(\frac{hc}{\lambda\, k\bar{T}^*\, t(s)}\right) - 1\right)^2} 4\pi s\, ds \tag{16}$$

Because the shape of the difference spectrum is only affected by the integral, the parameters in this model can be further reduced to one free parameter $\bar{T}^*$ with a normalization factor $C = \sqrt{\sum y_j y_{{\rm model},j} / \sum y^2_{{\rm model},j}}$, where y_j is the observed flux difference in band j and $y_{{\rm model},j}$ is the flux difference predicted by the model in band j given $\bar{T}^*$. The code integrates Equation (16) numerically from $6r_g$ out to 300 r_g.

We adopt both the P06 model and a model-independent power law $f_\lambda \propto \lambda^{-\alpha_\lambda}$ and perform least squares fitting weighted by the measurement error on our Δf SEDs. We calculate the goodness-of-fit (χ^2_ν) that is defined as

$$\chi^2_\nu = \frac{1}{N-2} \sum_j^N \left(\frac{y_j - C \cdot y_{{\rm model},j}}{\sigma_j} \right)^2, \tag{17}$$

where $N-2$ is the number of degrees of freedom of the fit. The 90% confidence interval of $\bar{T}^*$ is also calculated by varying $\bar{T}^*$ until $\Delta\chi^2 = 2.706$ if the source has more than four data points (two degrees of freedom).

4.5. Spectral Fitting

We describe in this section the method by which we measure redshift, line widths of Hβ and Mg II, and continuum luminosity from single epoch spectra to derive physical quantities such as black hole mass and accretion rate. All of our spectra are corrected for Galactic extinction using the Milky Way extinction curve from Cardelli et al. (1989) with $R_v = 3.1$ and the Schlegel et al. (1998) dust map.

For Hβ fitting, we first measure the continuum by fitting a linear function to two $\sim$60 Å wide sampling windows on the left of Hβ and on the right of [O III] $\lambda\lambda$4959, 5007 doublet. We remove the continuum and fit three Gaussians to the [O III] $\lambda\lambda$4959, 5007 and the narrow component of Hβ simultaneously. The linewidths and the redshift of the three Gaussian profiles are forced to change together, but the amplitudes of flux density are allowed to be free. We then use the redshift determined in this step as the systemic redshift to shift the spectrum back to its rest frame, and measure the narrow linewidth once again. The broad Hβ emission line is also modeled with a single Gaussian that is allowed to have a velocity offset. We fix the narrow component FWHM and fit both narrow and broad Hβ and [O III] $\lambda\lambda$4959, 5007 with four Gaussian profiles simultaneously.

For Mg II, we fit a linear function to the continuum on both sides of Mg II and subtract the continuum. We modeled Mg II with a single Lorentzian profile instead of a Gaussian because the Mg II lines in our spectra are better described by the former. We extract the redshift from Mg II line fitting if the object does not have cataloged redshift from SDSS. Note that we do not treat the Mg II line as Mg II $\lambda\lambda$2796, 2803 doublet because the double-peaked Mg II features in our spectra are unresolved at our spectral resolution. It is true that, by fitting one single line, we inevitably account for the narrow Mg II $\lambda\lambda$2796, 2803 contamination. Nevertheless, Shen et al. (2011) compared the broad Mg II FWHM measurement from treating Mg II as a single line and a doublet and found the result to be consistent. An example of the best-fit spectrum is shown in Figure 4. The redshift distribution of AGN and quasars are shown in Figure 5.

4.6. Accretion Rate

The bolometric luminosity ($L_{\rm bol}$) of quasars is usually measured by multiplying a bolometric correction to the luminosity density at 3000 Å or 5100 Å. However, this method is subject to the accuracy of flux calibration at a single wavelength. To take advantage of our broad wavelength coverage, we instead apply bolometric correction over a broader wavelength range by assuming the mean quasar SED in Richards et al. (2006).

We first calculate integrated UV/optical luminosity ($L_{\rm UV-opt}$) using photometry from *GALEX* NUV Gezari et al. (2013), CFHT *u* band, and *griz* from PS1 (Heinis et al. 2016).

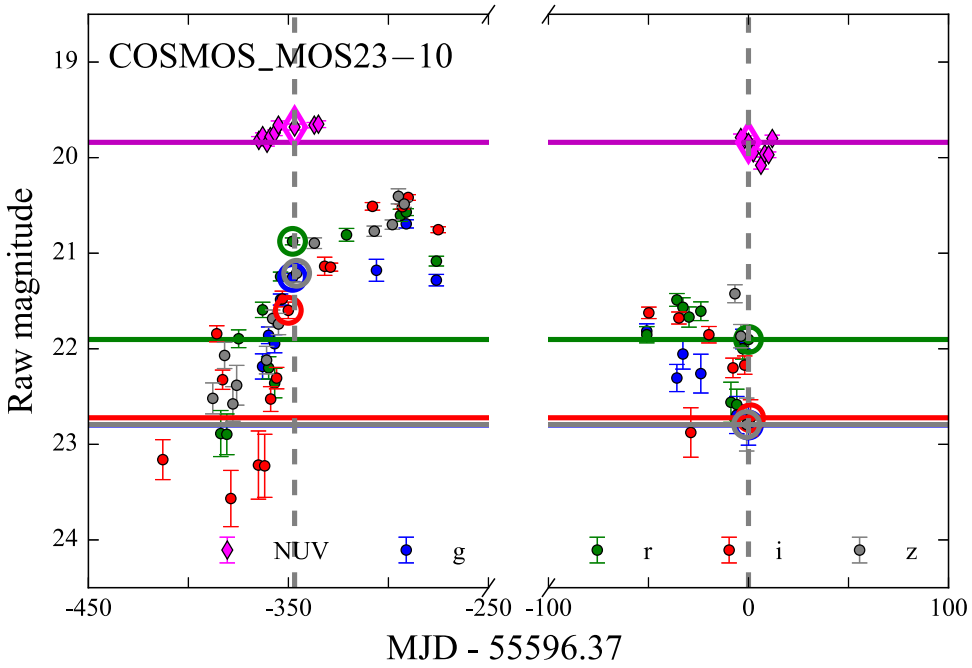

Figure 3. Light curve of COSMOS_MOS23-10 with epochs shown in time with respect to the reference epoch. Dashed lines mark the *GALEX* epochs of a bright and faint (reference) state. The *y*-axis shows the AB magnitude of the NUV/optical data in its original form. For *GALEX* NUV data, the raw magnitude includes flux from the host galaxy, whereas the PS1 optical points show the magnitudes of the template subtracted flux. Data circled are used in creating difference-flux SED. The raw magnitude in PS1 is shown as the brightness of a difference image, whereas in *GALEX* it is the brightness of the given epoch. The horizontal lines mark the raw magnitude of the reference with different colors indicating each band.

Note that, because AGNs suffer from host light contamination, we do not try to derive their bolometric luminosity and the accretion rate. We then scale $L_{\rm UV-opt}$ to $L_{\rm bol}$, using the mean quasar SED in Richards et al. (2006). Richards et al. (2006) constructed for a sample of 259 quasars detected by optical and MIR selection. Photometry data used in the construction of mean quasar SED are SDSS and the four bands of the Spitzer Infrared Array Camera were supplemented by near-IR, *GALEX*, VLA, and *ROSAT* data.

We convert the flux density f_ν from broadband photometry to luminosity L_ν using the following relation

$$L_{(1+z)\nu} = \frac{f_\nu}{1+z} \times 4\pi D_L^2, \tag{18}$$

where ν is the observed frequency and D_L is luminosity distance. An example of one of our quasar UV/optical SEDs is shown in Figure 6. The red squares shows the broadband photometry transformed into L_ν. The gray solid line is the mean quasar SED from Richards et al. (2006) normalized to enclose the same $\int L_\nu d\nu$ area as the red squares. We then interpolate νL_ν linearly between the effective frequency of NUV and z band with a spacing in $\Delta \log \nu$ of 0.05 dex and integrate $\int \nu L_\nu d \log \nu$ in rest frequency to obtain $L_{\rm UV-opt}$. The fractional contribution of $L_{\rm UV-opt}$ to $L_{\rm bol}$ is calculated using the mean quasar SED in Richards et al. (2006). Finally, we use this fraction to infer $L_{\rm bol}$ from $L_{\rm UV-opt}$. One thing to bear in mind is that the SEDs of quasars show significant scatter (Richards et al. 2006). Therefore, the value derived should be viewed in an average sense. The accretion rates are then calculated by assuming an accretion efficiency of $\eta \sim 0.06$ for a non-spinning black hole, where $L_{\rm bol} = \eta \dot{M}_{\rm accr} c^2$. The result is shown in Table 1.

4.7. Virial Mass

The reverberation mapping studies in the optical have yielded direct measurements of the sizes of the broad-line region ($R_{\rm BLR}$) as a function of continuum luminosity (Bentz et al. 2006, e.g.,). With one single-epoch spectrum, the black hole mass can be estimated with a measurement of $L_{\rm cont}$ and the broad-line FWHM, assuming that FWHM reflects the virialized motion of the line-emitting material. In general, the virial mass has the form:

$$\frac{M_{\rm bh}}{M_\odot} = A \left[\frac{\lambda L_\lambda}{10^{46}\ {\rm erg\ s^{-1}}} \right]^B \left[\frac{\rm FWHM}{\rm km\ s^{-1}} \right]^2, \tag{19}$$

where A and B are derived from empirical calibration against AGNs and λ is 5100 Å and 3000 Å for Hβ and Mg II, respectively.

We adopt the calibration of Trakhtenbrot & Netzer (2012). For Hβ, $A = 105$ and $B = 0.61$. For Mg II, $A = 5.6$ and $B = 0.62$. During spectral fitting, we measured redshift, FWHM of Hβ and Mg II, f_{5100}, and f_{3000} in the rest frame. We convert the flux density to the luminosity density using Equation (18).

The object class, the accretion rate, the black hole mass, the Eddington ratio, the FWHM of Mg II and Hβ of our sample are listed in Table 1.

5. RESULTS

We have compiled a sample of 24 sources that have a variability amplitude greater than 3σ in g band with well-aligned epochs across NUV and optical bands. One of the 24 sources, COSMOS_MOS27-07, shows the spectrum of an early-type galaxy but lacks emission lines typical of AGN so we do not include this source in our model fits (see Section 6.2

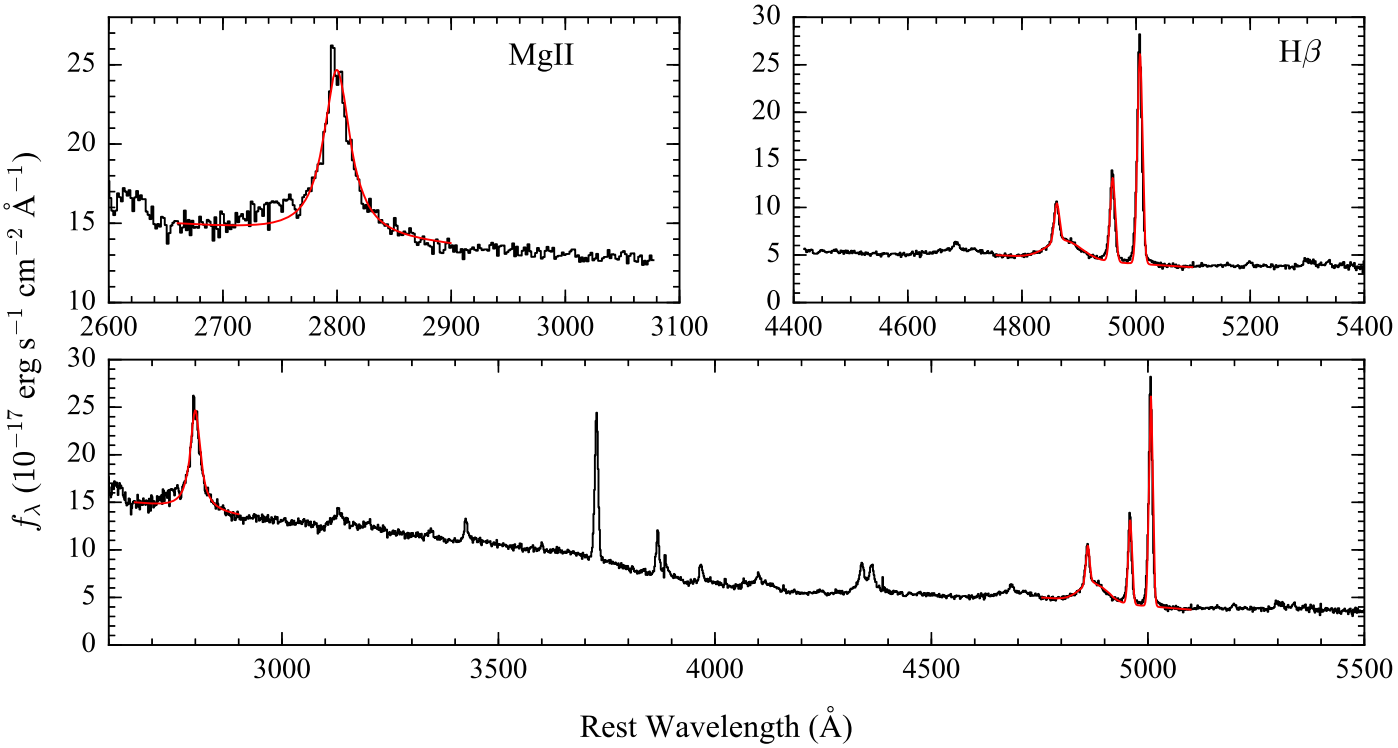

Figure 4. Optical spectrum of ELAISN1_MOS15-17 is shown by the black line while the best-fit model is shown by the red line. The upper two panels show the zoom-in view of Mg II and Hβ, respectively. The fitting procedure is described in Section 4.5.

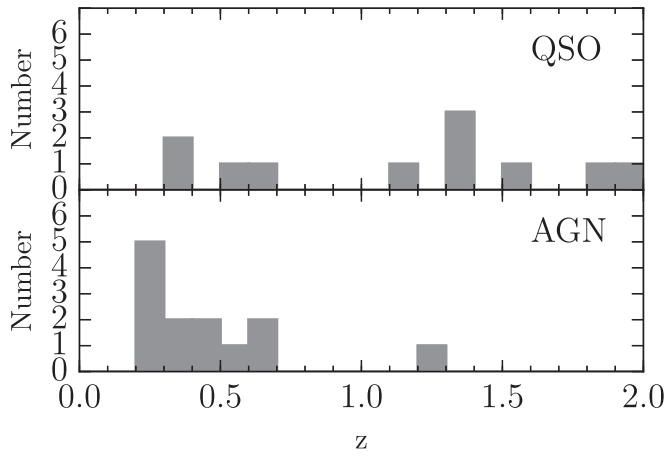

Figure 5. Redshift distribution of the AGNs and quasars in our sample. The redshift is measured as described in Section 4.5.

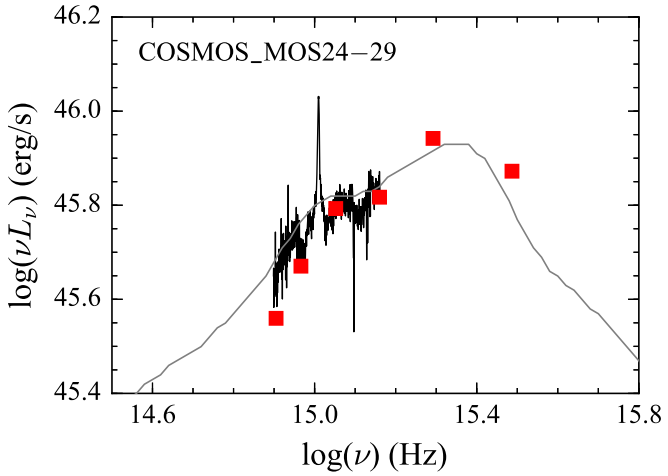

Figure 6. SED of a quasar in the sample. The red squares mark the luminosity transformed from *GALEX* NUV (Gezari et al. 2013) and the deep-stack *ugriz* photometry from Heinis et al. (2016) in rest frame. The black solid line is the spectrum of the source and the gray solid line is the mean quasar SED. Both gray and black lines are normalized so that the integrated luminosity matches that of the broadband photometry.

for discussion of the nature of this source). For the 23 active galaxies, we fit the difference flux SEDs following the method described in Section 4.4.

During the model fitting process, we noticed that the bands deviating the most from the P06 model tend to have strong broad emission lines within them. The contribution of broad emission line variability is discussed in Section 6.1. We suspect these bands may be contaminated by the emission from the BLR region and could affect our model fitting, because the model only accounts for the continuum variability that arises from the emission of the disk. In light of the potential contamination, we repeat model fitting by masking the bands associated with broad emission lines for sources with an original $\chi^2_\nu > 3.0$. Five sources show good agreement with the P06 model ($\chi^2_\nu > 3.0$) after we mask the broad emission line affected bands while the other six sources still have $\chi^2_\nu > 3.0$. The masked bands are shown as red crosses in Figures 7 and 11. The summary of the best-fit parameters can be found in Table 2.

We show the ΔfSED and the best-fit models for each well-fitted ($\chi^2_\nu \lesssim 3.0$) source and sources that exhibit deviation from the model ($\chi^2_\nu > 3.0$) in Figures 7 and 11. In the upper panel, the vertical axis is the difference-flux in flux density units in logarithmic scale, whereas the horizontal axis is the rest-frame

Table 1
Parameters Derived from Single-epoch Spectroscopy

GALEX objID	PS1ID	Class	z	$\log(L_{\rm bol})$[a] erg s^{-1}	$\dot{M}_{\rm accr}$ $M_\odot$ yr^{-1}	log10 ($M_{\rm bh}$) $M_\odot$	$L/L_{\rm Edd}$	FWHM (Hβ) km s^{-1}	FWHM (MgII) km s^{-1}	Telescope
CDFS_MOS05-19[b]	CfA10I080348	AGN	0.213	⋯	⋯	⋯	⋯	⋯	⋯	2DF Galaxy Survey
COSMOS_MOS23-02	CfA10D030238	QSO	1.507	45.83	1.96	9.06	0.05	⋯	5752.41	SDSS
COSMOS_MOS23-10	CfA10B010116	AGN	0.217	⋯	⋯	7.62	⋯	3274.5	⋯	SDSS
COSMOS_MOS23-18	CfA10L110530	QSO	0.664	44.84	0.20	8.12	0.04	⋯	3614.79	SDSS
COSMOS_MOS23-22	CfA11B130112	AGN	0.471	⋯	⋯	7.51	⋯	⋯	2046.52	MMT
COSMOS_MOS24-12	CfA10C020101	AGN	0.346	⋯	⋯	8.54	⋯	7164.72	⋯	SDSS
COSMOS_MOS24-25	CfA10L110532	QSO	0.500	44.55	0.10	7.13	0.22	⋯	1757.76	MMT
COSMOS_MOS24-29	CfA10D030011	QSO	1.319	46.12	3.83	8.97	0.12	⋯	3848.65	SDSS
COSMOS_MOS27-07	PS1-10uq	AGN[c]	0.312	⋯	⋯	⋯	⋯	⋯	⋯	MMT
COSMOS_MOS27-19	CfA10A000244	QSO	1.814	46.22	4.84	8.78	0.23	⋯	3293.83	SDSS
ELAISN1_MOS10-16	PS1-10amm	QSO	0.391	44.13	0.04	7.77	0.02	5369.35	⋯	MMT
ELAISN1_MOS12-05	CfA10H070227	AGN	0.267	⋯	⋯	8.18	⋯	5860.03	⋯	SDSS
ELAISN1_MOS12-09	CfA10I080066	QSO	1.369	45.32	0.60	8.31	0.09	⋯	2994.35	MMT
ELAISN1_MOS15-17	CfA10G060134	AGN	0.435	⋯	⋯	8.08	⋯	⋯	3029.09	MMT
ELAISN1_MOS16-27	CfA10G060158	AGN	0.558	⋯	⋯	7.96	⋯	⋯	6355.37	MMT
GROTH_MOS03-13	CfA10F050930	QSO	1.186	45.34	0.65	8.56	0.05	⋯	5035.06	MMT
GROTH_MOS03-21	CfA10D030207	AGN	1.296	⋯	⋯	7.68	⋯	⋯	2069.92	MMT
GROTH_MOS04-22	CfA10E040161	QSO	0.360	44.36	0.07	7.84	0.03	⋯	3693.61	SDSS
GROTH_MOS04-27	CfA10F050068	QSO	1.397	45.43	0.79	8.37	0.10	⋯	2971.59	SDSS
XMMLSS_MOS01-08	CfA10H071147	AGN	0.299	⋯	⋯	7.89	⋯	4355.55	⋯	SDSS
XMMLSS_MOS01-22	CfA10G061209	QSO	1.970	45.73	1.55	8.23	0.26	⋯	2980.13	MMT
XMMLSS_MOS02-06	PS1-10bet	AGN	0.692	⋯	⋯	8.72	⋯	⋯	6729.49	SDSS
XMMLSS_MOS04-06	CfA10H071018	AGN	0.606	⋯	⋯	7.69	⋯	⋯	2226.38	SDSS
XMMLSS_MOS05-25	CfA10H070606	AGN	0.276	⋯	⋯	0.0[d]	⋯	0.0	⋯	SDSS

Notes.
[a] We only calculate bolometric luminosity for point-like quasars because we cannot separate the host galaxy contribution from the AGN light in photometry.
[b] 2DFGS spectrum is not flux-calibrated.
[c] This source is classified as an AGN because of its extended morphology and stochastically varying light curve. However, this source does not have AGN emission lines in the spectrum. See the discussion in Section 6.2
[d] No measurement of black hole mass, because this source does not have broad emission lines.

wavelength in Å. The red line shows the best-fit result from the standard thin disk model, and the green line shows the best-fit result of a power law. The shaded area is bounded by two curves corresponding to the upper (steep) and lower (flat) limit of $\bar{T}^*$ and is only plotted for objects with $\chi^2_\nu \lesssim 3.0$. We also overplot the spectra for each source in gray in Figures 7 and 11 in logarithmic scale. The bottom panel shows the residual divided by the uncertainty (σ) for each band, where red squares are from the P06 model and the green triangles are from the power-law model.

It is worth noting that, for our sample, the P06 model performs significantly better than the power law in terms of χ^2_ν and the P06 model fits qualitatively well to the data points in Figure 11 despite their larger χ^2_ν values.

For the 17 out of 23 objects that are well described by the model, the distribution of the best-fit mean characteristic temperatures $\bar{T}^*$ is shown in the upper panel of Figure 8. The median $\bar{T}^*$ of our sample is 1.2×10^5 K, which is higher than the mean characteristic temperature of 92,000 K found for a composite difference spectrum constructed from SDSS quasars (Pereyra et al. 2006). However, the difference composite spectrum in Pereyra et al. (2006) is not corrected for Galactic extinction, meaning the underlying difference spectrum may be bluer, and therefore could imply a hotter disk temperature than the value derived in Pereyra et al. (2006).

The bottom panel of Figure 8 shows the distribution of best-fit power-law indices. A standard accretion disk model predicts a $f_\nu \propto \nu^{1/3}$ spectrum for intermediate ν between the frequencies corresponding to the innermost disk and the Rayleigh–Jeans limit. This value translates to a spectral index α_λ of ≈ 2.33. Although the bluer-when-brighter trend can be explained as an intrinsic effect of AGN under the assumption of an accretion disk model, real AGN spectra rarely match this value. Instead, this spectral index is more often seen toward difference spectra of AGN. For instance, Wilhite et al. (2005) found α_λ of 1.35 and 2.00 for the average quasar spectrum and the average quasar difference spectrum, respectively, using SDSS spectra without correcting for reddening due to Galactic extinction. Vanden Berk et al. (2001) found a slightly bluer α_λ of 1.56 for composite quasar spectrum after correcting for Galactic extinction, but is still not as blue as the theoretical prediction of a thin accretion disk. The composite quasar difference spectrum having a steeper spectral index than the composite quasar spectrum implies that the variable component may come directly from the disk, and that taking the difference flux isolates the radiation from the disk component more cleanly. Our finding of a median of the best-fit power-law index $\alpha_\lambda \approx 2.1$ is consistent with the spectral index of the SDSS geometric mean composite difference spectrum of quasars in Ruan et al. (2014) and is close to the standard thin disk value of 2.33.

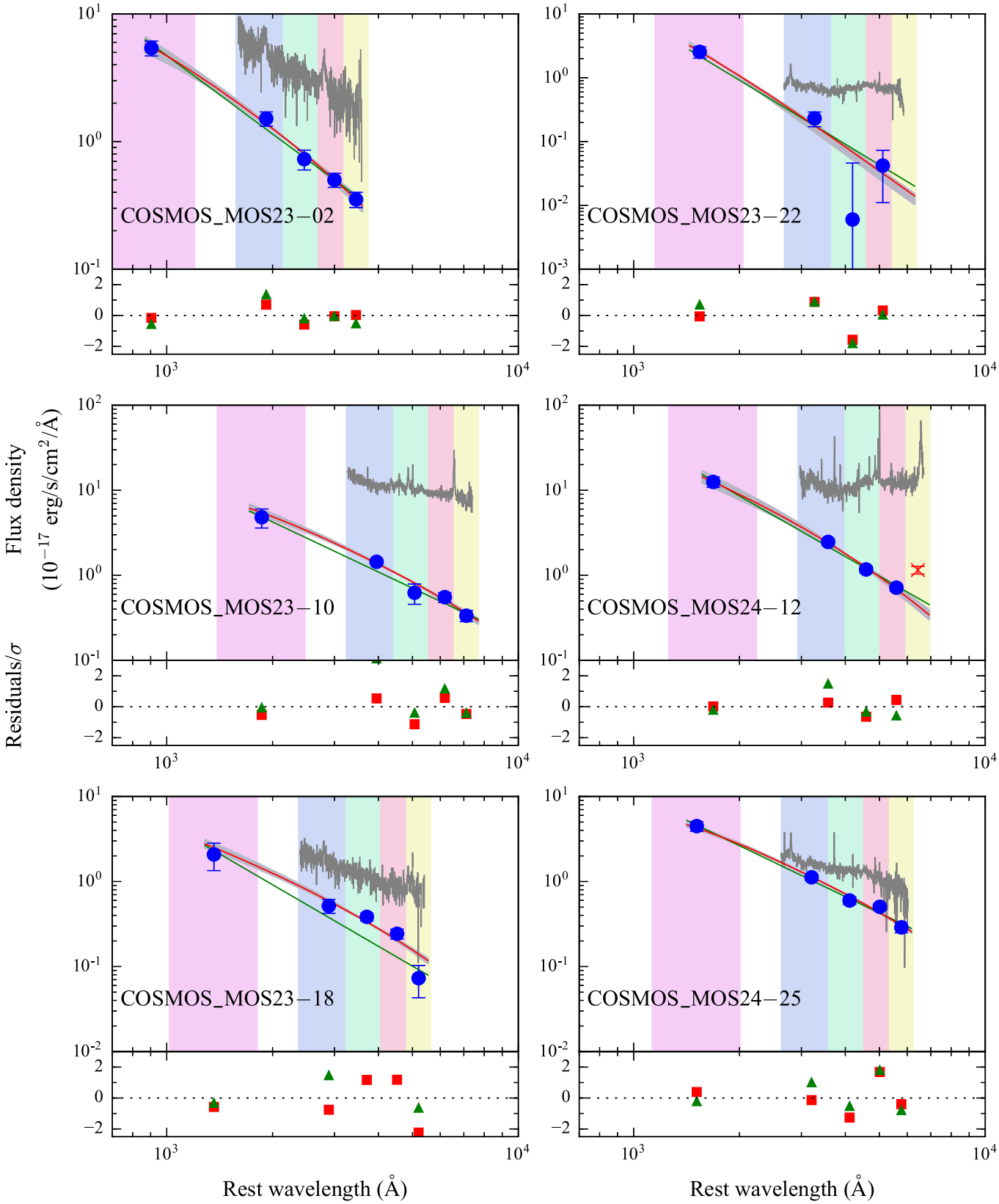

Figure 7. Difference-flux SEDs and the best-fit results of the 17/23 sources with $\chi^2_\nu < 3$ in the sample. In the upper panel of each subplot, the red line shows the best fit of P06 model and green line shows the best fit of a simple power law. The horizontal axis is the rest wavelength in Å, whereas the vertical axis is the difference-flux on a logarithmic scale. The shaded area is bounded by two curves corresponding to the 1σ upper (steep) and lower (flat) limits of $\bar{T}^*$. The filter transmission curves for *NUV*, *g*, *r*, *i*, *z* shifted into the rest frame are colored in the background. The optical spectra are also plotted in gray for each source, in logarithmic scale. The lower panel shows the residuals of the model fit divided by the uncertainty of each measurement, where the red squares are from the P06 model and the green triangles are from a power law.

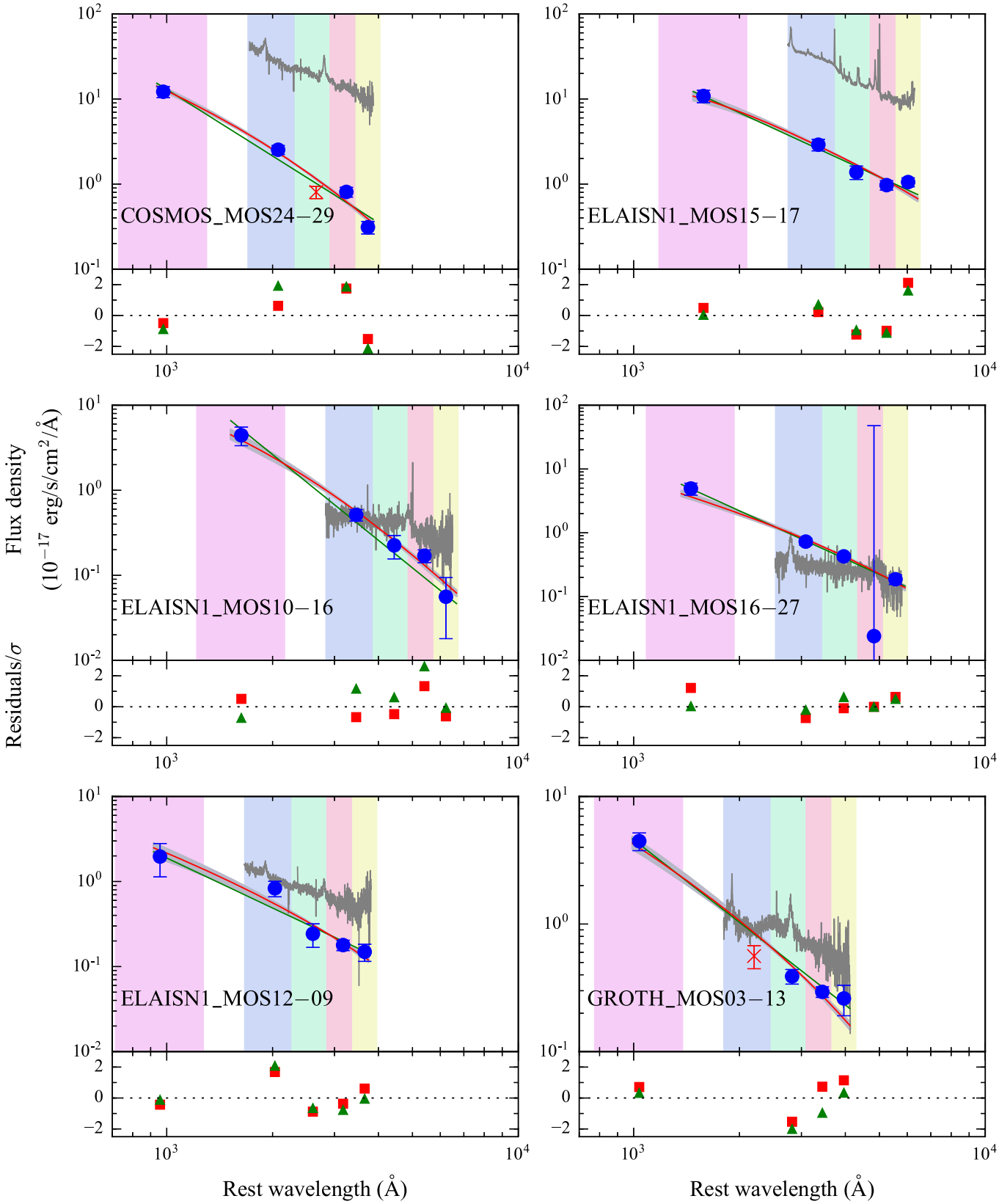

Figure 7. (Continued.)

The classic thin-disk model predicts the characteristic temperature T^* as a function of accretion rate and black hole mass (see Equation (4)). For example, for a quasar accreting at the rate of 1 $M_\odot$ yr^{-1} with a mass of 10^9 $M_\odot$, a standard accretion disk predicts a characteristic temperature of 70,000 K. As a sanity check, we also calculate the characteristic temperature T^* using the accretion rates and the black hole masses derived in Sections 4.6 and 4.7 using photometry and

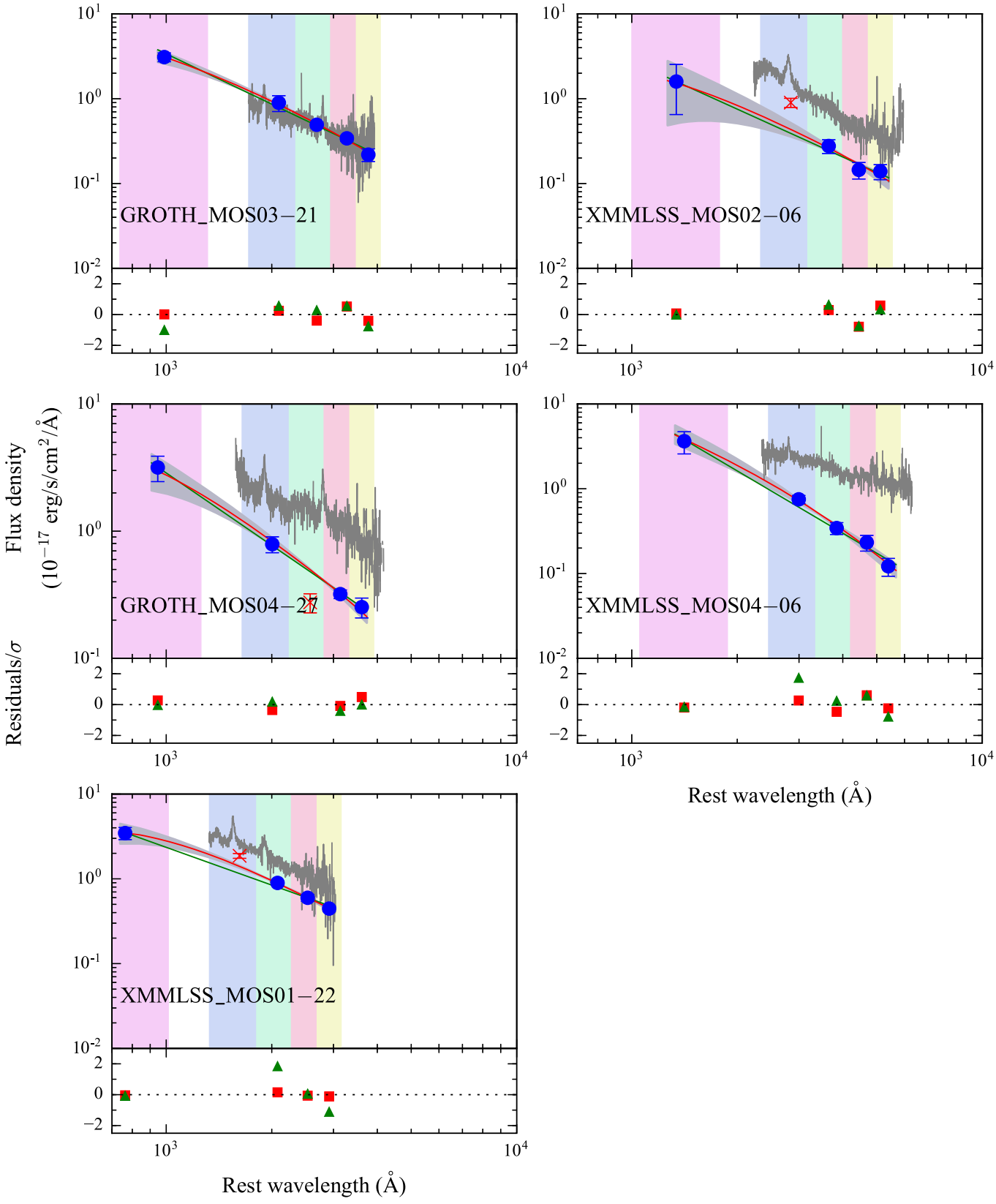

Figure 7. (Continued.)

single-epoch spectroscopy. The distribution of T^* and $\bar{T}^*$ are plotted in Figure 9. The data are binned into 0.1 dex intervals. Note that we only plotted $\bar{T}^*$ for point-like quasars, to avoid estimating the accretion rates for extended sources, which will have systematic uncertainties in $L_{\rm bol}$ due to host light contamination. Although we do not see a one-to-one correlation in the characteristic temperature T^* and $\bar{T}^*$, the distribution of T^* and $\bar{T}^*$ are consistent with each other; therefore, they

Table 2
Best-fit Parameters of the Sample

GALEX ID	$\bar{T}^*$ (10^5 K)	χ_ν^{2a}	α_λ	χ_ν^{2b}	Δt (days)[c]
CDFS_MOS05-19	0.58	10.87	$1.97^{+0.18}_{-0.44}$	33.6	330
COSMOS_MOS23-02	$1.42^{+0.28}_{-0.27}$	0.28	$2.04^{+0.19}_{-0.20}$	2.48	355
COSMOS_MOS23-10	$0.67^{+0.10}_{-0.07}$	0.79	$2.11^{+0.18}_{-0.28}$	5.42	347
COSMOS_MOS23-18	$1.06^{+0.17}_{-0.12}$	2.82	$1.91^{+0.48}_{-0.12}$	14.11	347
COSMOS_MOS23-22	$5.04^{+12.6}_{-0.62}$	1.64	$3.26^{+0.02}_{-0.14}$	5.29	359
COSMOS_MOS24-12	$1.25^{+0.26}_{-0.23}$	0.35	$2.43^{+0.18}_{-0.22}$	2.5	355
COSMOS_MOS24-25	$0.76^{+0.06}_{-0.04}$	1.59	$1.94^{+0.20}_{-0.16}$	4.75	347
COSMOS_MOS24-29	$2.42^{+0.19}_{-0.15}$	3.00	$2.52^{+0.26}_{-0.10}$	14.96	353
COSMOS_MOS27-07[d]	1.18	5.08	2.10	14.17	343
COSMOS_MOS27-19	1.08	4.48	$1.42^{+0.22}_{-0.20}$	4.84	355
ELAISN1_MOS10-16	$1.89^{+0.30}_{-0.22}$	1.03	$2.78^{+0.44}_{-0.32}$	2.3	355
ELAISN1_MOS12-05	1.14	3.57	$2.66^{+0.34}_{-0.38}$	2.45	355
ELAISN1_MOS12-09	$1.52^{+0.24}_{-0.36}$	1.43	$2.35^{+0.14}_{-0.48}$	6.42	48
ELAISN1_MOS15-17	$0.67^{+0.11}_{-0.07}$	2.43	$1.85^{+0.26}_{-0.22}$	5.61	306
ELAISN1_MOS16-27	$1.18^{+0.18}_{-0.14}$	0.82	$2.42^{+0.30}_{-0.36}$	0.27	304
GROTH_MOS03-13	$1.64^{+0.26}_{-0.19}$	2.37	$2.26^{+0.24}_{-0.28}$	2.03	362
GROTH_MOS03-21	$1.12^{+0.22}_{-0.20}$	0.21	$1.88^{+0.16}_{-0.18}$	1.60	356
GROTH_MOS04-22	1.09	4.32	$2.32^{+0.18}_{-0.20}$	5.09	356
GROTH_MOS04-27	$1.14^{+0.40}_{-0.32}$	0.22	$1.93^{+0.27}_{-0.32}$	0.11	316
XMMLSS_MOS01-08	1.41	5.22	$2.46^{+0.20}_{-0.08}$	22.2	331
XMMLSS_MOS01-22	$0.97^{+0.18}_{-0.15}$	0.02	$1.58^{+0.16}_{-0.20}$	3.96	317
XMMLSS_MOS02-06	$0.78^{+0.61}_{-0.38}$	0.53	$1.93^{+0.50}_{-0.48}$	1.08	329
XMMLSS_MOS04-06	$1.54^{+0.54}_{-0.41}$	0.25	$2.56^{+0.26}_{-0.34}$	2.94	325
XMMLSS_MOS05-25	1.08	3.73	$2.35^{+0.12}_{-0.12}$	4.25	323

Notes. Best-fit parameters of the sample after masking bands with strong broad emission lines. The masked bands are shown as red crosses in Figures 7 and 11.
[a] Reduced χ^2 for the change in accretion rate (P06) model.
[b] Reduced χ^2 for the power-law model.
[c] The time interval between the bright and faint epochs for each object.
[d] This source has a quiescent host galaxy. See the discussion in Section 6.2.

follow the expectations for an accretion disk with the ranges of $M_{\rm bh}$ and $\dot{M}_{\rm accr}$ inferred for the quasars in our sample.

6. DISCUSSION

6.1. Emission-line Variability

Before masking the bands containing broad emission lines, 11/23 sources in Table 2 have large χ_ν^2 values and are clearly ill-fitted by the change in accretion rate model. One likely explanation is that the the ΔfSEDs of these objects are contaminated by emission line variability. Broad emission lines are known to both vary in flux and in profile (Wamsteker et al. 1990; Kassebaum et al. 1997, e.g.,). In extreme cases, such as a "changing-look" AGN that involves the sudden appearance or disappearance of the broad Balmer lines on the timescale of years (e.g., Shappee et al. 2014), the broad band flux may experience a dramatic change due to the change in emission line flux. Using XMMLSS_MOS01-22 as an example, the difference-flux in g band deviates from the model prediction by ∼30% (Figure 7), which would inevitably result in a poor model fit if we force to fit all bands. In fact, Wilhite et al. (2005) also reported that broad emission lines could vary by 30% as much as the continuum in the spectroscopic variability study of SDSS quasars. It is important to recognize that the amount of flux change contributed by a broad AGN emission line can be non-negligible compared to the change in continuum in broadband.

We find that masking the broad-emission-line contaminated bands can improve the poor model fit. Although only 5/11 originally ill-fitted sources have $\chi_\nu^2 < 3.0$ after applying band masks, most of the sources have a qualitatively good model fit even when having $\chi_\nu^2 > 3.0$ (Figure 11).

6.2. COSMOS_MOS27-07

While examining the spectra, we found one source, COSMOS_MOS27-07, that lacks common AGN emission lines even though classified as an AGN from its morphology and light curve. The light curve of COSMOS_MOS27-07 is shown in Figure 10.

COSMOS_MOS27-07 resides in an early-type host galaxy with colors $u - g = 1.71$ and $g - r = 1.64$. The *GALEX* TDS catalog reports a maximum variability amplitude ($\Delta m_{\rm max}$) of >1.37 mag, with significant variability on timescales of 1–2 years (Gezari et al. 2013). It is unlikely that such amplitude of variability in NUV is caused by core-collapse supernovae because their NUV light curves are powered by expanding shock-heated ejecta, which cool quickly with time.

Such variability can be powered by a tidal disruption event (TDE), which features persistent emission in the UV ($\gtrsim$1 year). However, the long-term plateau in the *GALEX* light curve is unlike the power-law decay observed in TDEs. Observations in X-ray wavelengths may reveal if this object is a X-ray bright, optically normal galaxy (XBONG, Comastri et al. 2002).

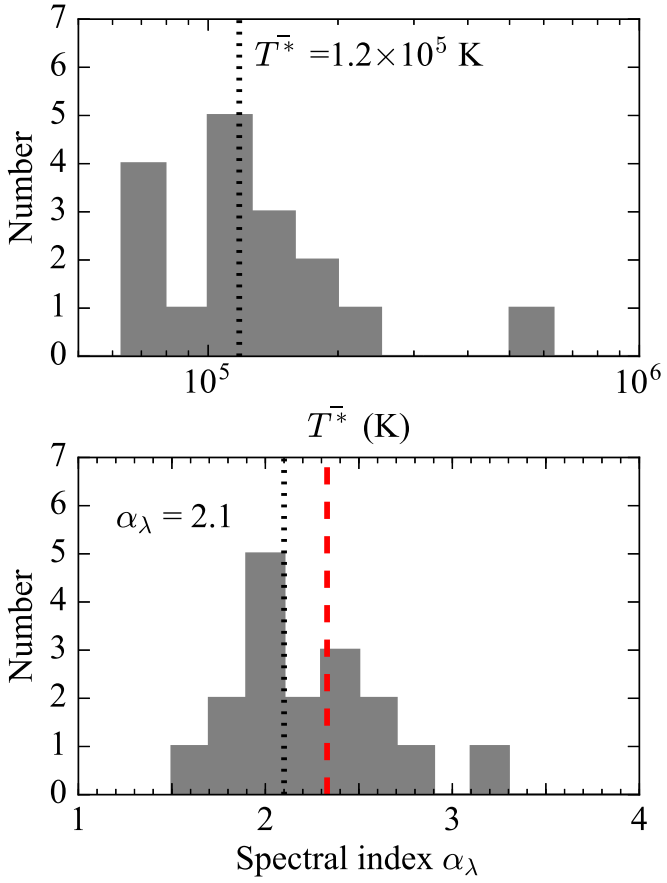

Figure 8. Upper panel: the distribution of best-fit mean characteristic temperature $\bar{T}^*$. Bottom panel: the distribution of spectral index α_λ. Red dashed line shows the theoretical value of 2.33.

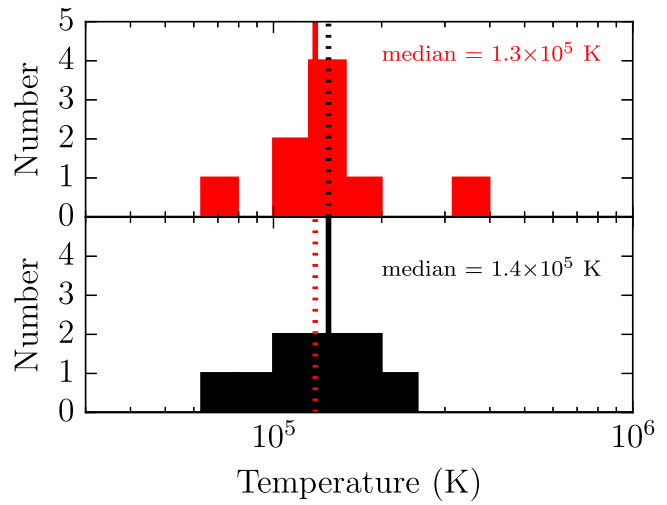

Figure 9. Distribution of $\bar{T}^*$ (black) and T^* (red), where $\bar{T}^*$ is calculated from fitting the Δf SEDs to the P06 model and T^* is calculated from substituting accretion rate and black hole mass into Equation (4). Note that we only include the 12 sources that are classified as quasars to avoid accounting for galaxy light contamination. Although the two histograms seem to have similar temperature distribution, there is no clear trend in the scatter plot of $\bar{T}^*$ vs. T^*.

6.3. Timescales

Due to the time sampling of *GALEX* TDS, the Δf SEDs in our active galaxy sample probe a variability timescale of about a year. An assumption in our model is that enough time has elapsed for the the disk to adjust to a different mass accretion rate. However, the timescale associated with mass inflow, the viscous timescale, is on the order of 1000 years assuming a characteristic disk with thickness $h/r = 0.01$, $M = 10^8\,M_\odot$ and $\alpha = 0.1$ at $r \sim 100 r_g$, where $r_g \equiv 2GM/c^2$ is the gravitational radius. In general, the viscous timescale is given by:

$$\tau = \left(\frac{h}{r}\right)^{-2} \frac{1}{\alpha\Omega}, \tag{20}$$

where h/r is the thickness of the disk in units of the radius, α the viscosity, and Ω the angular velocity. To match the timescale we observed, the mass accretion perturbation must originate from a radius close to the UV/optical emitting region or have a much thicker disk ($\tau_{\rm visc} \sim 10$ years if $h/r = 0.1$).

As pointed out in Pereyra et al. (2006), the observed months-to-years variability timescales are more consistent with the sound-speed timescale of an accretion disk. Changes in accretion rate might result in density and pressure perturbations, which can propagate across a proportion of the disk as sound waves. The DRW model, proposed by Kelly et al. (2009) to describe the optical variability seen in quasar light curves, also shows fits with a characteristic timescale of ∼200 days that is consistent with the thermal timescale.

Another possibility is that the UV/optical variability is driven by reprocessing of X-ray photons from the inner disk. Under the assumption of a classic thin disk, the UV and optical spectrum arise predominately from spatially separated locations. Therefore, one would expect the time-lag between different bands to be observed as a result of signal propagation. In fact, inter-band correlations were found in short timescale variability in NGC 2617 and NGC 5548 (Shappee et al. 2014; Fausnaugh et al. 2015) as evidence supporting the X-ray reprocessing scenario. Following an outburst in NGC 2617, the galaxy has shown disk emission in the UV/optical lagging the X-ray by two to three days (Shappee et al. 2014). This time lag is consistent with the light crossing time from the inner X-ray emitting region to the outer UV/optical emitting region. Although the UV and optical variability seem to correlate well with the X-rays on short (∼day) timescales, previous studies also reported the presence of pronounced long timescale (∼year) variability in the optical, but not in the X-rays (Breedt et al. 2009; McHardy et al. 2014), suggesting an independent mechanism contributing to the optical variability.

Unfortunately, with this study, we can not differentiate between the steady-state spectrum of an X-ray-illuminated source from that of a steady-state accretion disk, because they have the same radial dependence (r^{-3}). Simultaneous X-ray and UV/optical observations on the light-crossing timescale (∼days), not available in this study, would be required to distinguish between these two models.

6.4. Inhomogeneous Disk Model

The main weakness of the P06 model lies in the discrepancy between the observed continuum variability timescales, and the much longer timescales over which an accretion rate can change globally in the disk (see Section 6.3 for discussion). Inspired by the better agreement with thermal timescales (Kelly et al. 2009), Dexter & Agol (2011) proposed an inhomogeneous disk model in which the disk is separated into multiple zones that each vary on the thermal timescale, with an independent temperature fluctuation conforming to the DRW

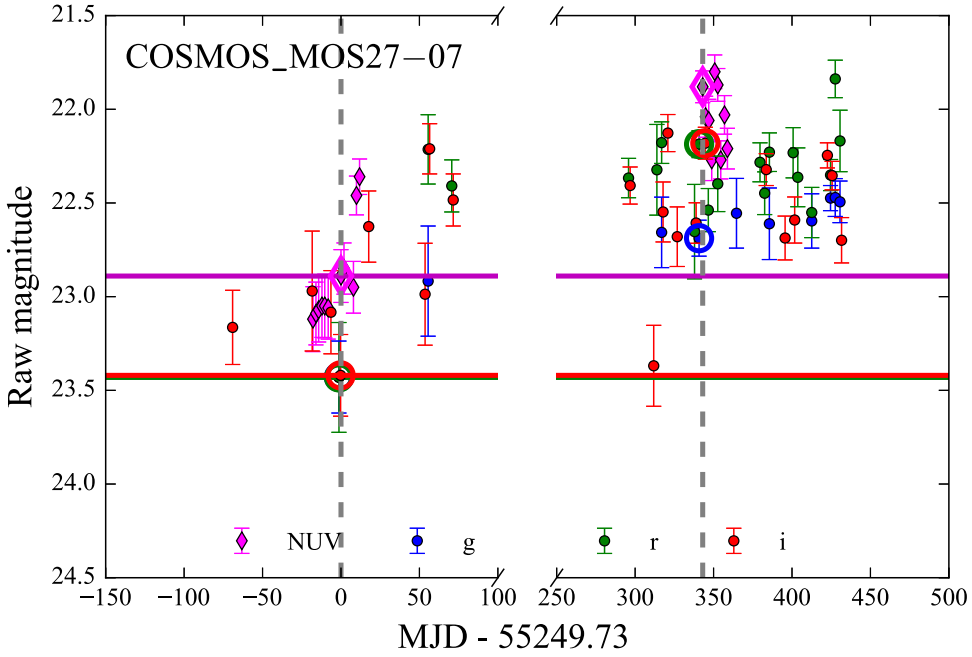

Figure 10. Light curve of COSMOS_MOS27-07 with epochs shown in time with respect to the reference epoch. The notations are the same as defined in Figure 3.

process. Furthermore, Dexter & Agol (2011) find that the localized temperature fluctuation model predicts a higher flux at shorter wavelength ($\lambda < 1000$ Å) than the standard thin disk model, and can better describe the composite *HST* quasar spectrum from Zhang et al. (1997).

Ruan et al. (2014) fitted a composite *relative* variability spectrum, created by dividing the composite difference spectrum by the composite quasar spectrum, in the wavelength range of $\lambda = 1500$–6000 Å. They found that the composite relative variability spectrum is better described by the thermal fluctuation model than the standard thin disk model, assuming a fixed 5% increase in the mass accretion rate for the standard thin disk model. Unfortunately, we cannot directly compare our results by fitting a "relative variability" SED, because of emission line contamination in our broadband photometry. However, the motivation for constructing the relative variability spectrum in Ruan et al. (2014) was to get rid of the effect of internal AGN extinction. However, when we measure the spectral indices of the single-epoch optical spectra of our active galaxy sample, we find only 5 out of 23 targets with a spectral index redder than the spectral index of the SDSS quasar composite $\alpha_\lambda \approx 1.56$ (Vanden Berk et al. 2001) that might indicate the presence of internal extinction. In addition, we suspect that comparing the composite relative variability spectrum to the model difference spectra divided by a low-state disk model is not a fair comparison, because the low-state disk model, as we discussed in Section 5, is much bluer than the observed composite quasar spectrum. In sum, we doubt that internal extinction is a significant issue for our sample, and we find a good agreement between the P06 model and our variability SEDs.

Recent work from Cai et al. (2016) shows the revised thermal fluctuation model with radius-dependent characteristic timescales also shows noticeable departures from the prediction of a standard thin disk model at $\lambda \lesssim 1000$ Å. However, because the shortest rest wavelength probed in our sample is ≈800 Å, we cannot look for this characteristic signature. Our analysis shows that, on an object-by-object basis, the P06 model is an appropriate description of the individual ΔfSEDs of the AGNs and quasars. We do not find the need to invoke the thermal fluctuation model in most of the cases. However, the NUV flux in ELASN1_MOS12-05 and GROTH_MOS03-13 is indeed higher than predicted by the P06 model, introducing localized thermal fluctuations might be able to explain the flux excess in NUV.

7. SUMMARY

We analyze the spectral variability of a sample of 24 *GALEX* TDS NUV variability selected sources with large amplitude optical variability (difference flux S/N > 3 in the $g_{\rm P1}$ band) in the PS1 Medium Deep Survey. We gathered single-epoch spectra for the sample, and found 23 out of 24 sources have emission lines characteristic of an unobscured AGN. The bluer-when-brighter trend is observed across our sample. We have fitted a standard thin disk model with variable accretion rates, as well as a simple power law to the spectral shape of the observed difference-flux SEDs (ΔfSEDs). We have also measured accretion rate, black hole mass, and Eddington ratio for our sample using photometric and spectroscopic data. The mean timescale of UV/optical variability we are probing is one year. We find the change in accretion rate model generally describes the ΔfSEDs better than a simple power law. Our results can be summarized as follows.

1. The median of the best-fit mean characteristic temperature $\bar{T}^*$ is 1.2×10^5 K. The distribution of $\bar{T}^*$ is consistent with the distribution of the characteristic temperature T^* (median 1.3×10^5 K) obtained from independently measured accretion rates and black hole masses.
2. The best-fit power-law indices α_λ of the difference spectra have a median of 2.1, which is consistent with the value previously found in Wilhite et al. (2005) and Ruan et al. (2014) and is close to the spectral index $\alpha_\lambda \approx 2.33$ of a classical thin disk.

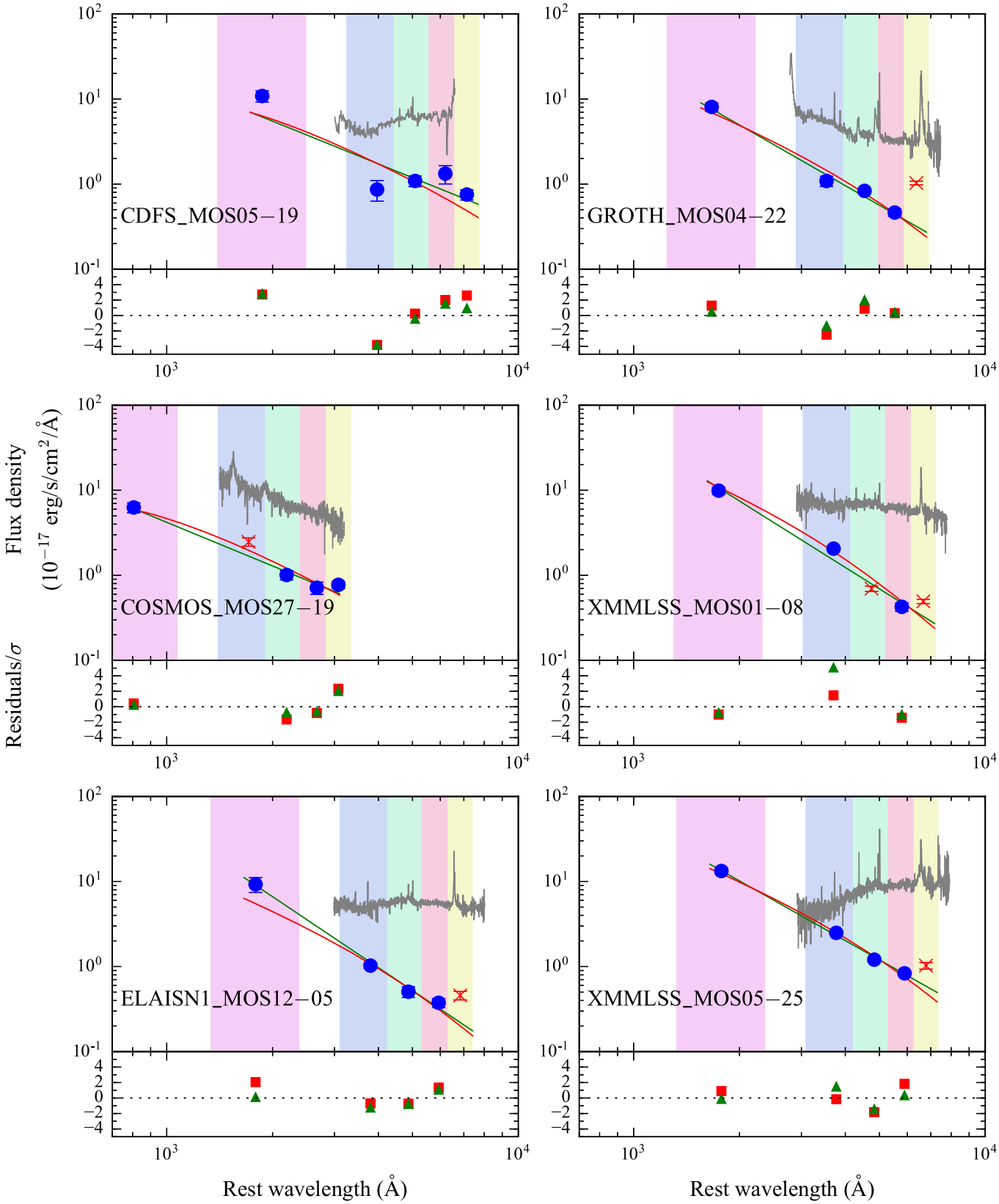

Figure 11. Difference-flux SEDs and the best-fit results of the 6/23 sources that are poorly fitted by the model ($\chi^2_\nu > 3$). The notations are the same as in Figure 7.

Our results suggest that the spectral shape of large-amplitude AGN variability on long timescales (∼years) is described well by a thin steady-state disk with a variable accretion rate. However, at the wavelength range and timescales we are probing, we cannot distinguish between this simple variable accretion disk model, and a more complicated disk model with localized thermal fluctuation zones, or X-ray reprocessing. Broadband monitoring of AGN on the timescale of days from

the soft X-rays to optical would help distinguish between these scenarios.

We thank the anonymous referee for valuable comments and suggestions that helped to improve this paper. S.G. was supported in part by NSF CAREER grant 1454816. Some of the observations reported here were obtained at the MMT Observatory, a joint facility of the Smithsonian Institution and the University of Arizona. We thank R. Foley for his contribution to the PS1 transients program. The Pan-STARRS1 Surveys (PS1) have been made possible through contributions of the Institute for Astronomy, the University of Hawaii, the Pan-STARRS Project Office, the Max-Planck Society and its participating institutes, the Max Planck Institute for Astronomy, Heidelberg and the Max Planck Institute for Extraterrestrial Physics, Garching, The Johns Hopkins University, Durham University, the University of Edinburgh, Queen's University Belfast, the Harvard-Smithsonian Center for Astrophysics, the Las Cumbres Observatory Global Telescope Network Incorporated, the National Central University of Taiwan, the Space Telescope Science Institute, the National Aeronautics and Space Administration under Grant No. NNX08AR22G issued through the Planetary Science Division of the NASA Science Mission Directorate, the National Science Foundation under Grant No. AST-1238877, and the University of Maryland.

REFERENCES

Abazajian, K., Adelman-McCarthy, J. K., Agüeros, M. A., et al. 2003, AJ, 126, 2081
Baldry, I. K., Glazebrook, K., Baugh, C. M., et al. 2002, ApJ, 569, 582
Bentz, M. C., Denney, K. D., Cackett, E. M., et al. 2006, ApJ, 651, 775
Breedt, E., Arévalo, P., McHardy, I. M., et al. 2009, MNRAS, 394, 427
Cai, Z.-Y., Wang, J.-X., Gu, W.-M., et al. 2016, arXiv:1605.03185
Cardelli, J. A., Clayton, G. C., & Mathis, J. S. 1989, ApJ, 345, 245
Colless, M., Peterson, B. A., Jackson, C., et al. 2003, arxiv:astro-ph/0306581
Comastri, A., Brusa, M., Ciliegi, P., et al. 2002, arxiv:astro-ph/0203019
Dawson, K. S., Schlegel, D. J., Ahn, C. P., et al. 2013, AJ, 145, 10
Dexter, J., & Agol, E. 2011, ApJL, 727, L24
Fabricant, D., Fata, R., Roll, J., et al. 2005, PASP, 117, 1411
Fausnaugh, M. M., Denney, K. D., Barth, A. J., et al. 2015, arXiv:1510.05648
Fitzpatrick, E. L. 1999, PASP, 111, 63
Gezari, S., Martin, D. C., Forster, K., et al. 2013, ApJ, 766, 60
Heinis, S., Kumar, S., Gezari, S., et al. 2016, ApJ, 821, 86
Hirose, S., Blaes, O., & Krolik, J. H. 2009, ApJ, 704, 781
Janiuk, A., & Misra, R. 2012, A&A, 540, A114
Jiang, Y.-F., Stone, J. M., & Davis, S. W. 2013, ApJ, 778, 65
Kaiser, N., Burgett, W., Chambers, K., et al. 2010, Proc. SPIE, 7733, 77330E
Kassebaum, T. M., Peterson, B. M., Wanders, I., et al. 1997, ApJ, 475, 106
Kelly, B. C., Bechtold, J., & Siemiginowska, A. 2009, ApJ, 698, 895
Kokubo, M. 2015, MNRAS, 449, 94
Kokubo, M., Morokuma, T., Minezaki, T., et al. 2014, ApJ, 783, 46
Krolik, J. H., Horne, K., Kallman, T. R., et al. 1991, ApJ, 371, 541
Kumar, S., Gezari, S., Heinis, S., et al. 2015, ApJ, 802, 27
Li, S.-L., & Cao, X. 2008, MNRAS, 387, L41
MacLeod, C. L., Ivezić, Ž., Kochanek, C. S., et al. 2010, ApJ, 721, 1014
Magnier, E. 2006, in The Advanced Maui Optical and Space Surveillance Technologies Conf., ed. S. Ryan (Maui, HI: MEDB), 50
McHardy, I. M., Cameron, D. T., Dwelly, T., et al. 2014, MNRAS, 444, 1469
Pereyra, N. A., Vanden Berk, D. E., Turnshek, D. A., et al. 2006, ApJ, 642, 87
Rest, A., Scolnic, D., Foley, R. J., et al. 2014, ApJ, 795, 44
Rest, A., Stubbs, C., Becker, A. C., et al. 2005, ApJ, 634, 1103
Richards, G. T., Lacy, M., Storrie-Lombardi, L. J., et al. 2006, ApJS, 166, 470
Ruan, J. J., Anderson, S. F., Dexter, J., & Agol, E. 2014, ApJ, 783, 105
Sakata, Y., Morokuma, T., Minezaki, T., et al. 2011, ApJ, 731, 50
Schlegel, D. J., Finkbeiner, D. P., & Davis, M. 1998, ApJ, 500, 525
Schmidt, K. B., Rix, H.-W., Shields, J. C., et al. 2012, ApJ, 744, 147
Shakura, N. I., & Sunyaev, R. A. 1973, A&A, 24, 337
Shappee, B. J., Prieto, J. L., Grupe, D., et al. 2014, ApJ, 788, 48
Shen, Y., Richards, G. T., Strauss, M. A., et al. 2011, ApJS, 194, 45
Tonry, J. L., Stubbs, C. W., Lykke, K. R., et al. 2012, ApJ, 750, 99
Trakhtenbrot, B., & Netzer, H. 2012, MNRAS, 427, 3081
Vanden Berk, D. E., Richards, G. T., Bauer, A., et al. 2001, AJ, 122, 549
Vanden Berk, D. E., Wilhite, B. C., Kron, R. G., et al. 2004, ApJ, 601, 692
Wamsteker, W., Rodriguez-Pascual, P., Wills, B. J., et al. 1990, ApJ, 354, 446
Wilhite, B. C., Vanden Berk, D. E., Kron, R. G., et al. 2005, ApJ, 633, 638
Winkler, H., Glass, I. S., van Wyk, F., et al. 1992, MNRAS, 257, 659
Wyder, T. K., Martin, D. C., Schiminovich, D., et al. 2007, ApJS, 173, 293
Zheng, W., Kriss, G. A., Telfer, R. C., Grimes, J. P., & Davidsen, A. F. 1997, ApJ, 475, 469